The Astrophysical Journal, 707:1595–1609, 2009 December 20 doi:10.1088/0004-637X/707/2/1595

THE BIMODAL GALAXY STELLAR MASS FUNCTION IN THE COSMOS SURVEY TO $z \sim 1$: A STEEP FAINT END AND A NEW GALAXY DICHOTOMY

N. Drory[1], K. Bundy[2,14], A. Leauthaud[3,4], N. Scoville[5], P. Capak[5,6], O. Ilbert[7], J. S. Kartaltepe[8], J. P. Kneib[7], H. J. McCracken[9], M. Salvato[5,10], D. B. Sanders[11], D. Thompson[12], and C. J. Willott[13]
[1] Max-Planck Institut für extraterrestrische Physik, Giessenbachstraße, 85748 Garching, Germany; drory@mpe.mpg.de
[2] Astronomy Department, 601 Campbell Hall, University of California at Berkeley, Berkeley, CA 94720, USA
[3] Lawrence Berkeley National Laboratory, 1 Cyclotron Road, Berkeley, CA 94720, USA
[4] Berkeley Center for Cosmological Physics, University of California, Berkeley, CA 94720, USA
[5] California Institute of Technology, MC 105-24, 1200 East California Boulevard, Pasadena, CA 91125, USA
[6] Spitzer Science Center, California Institute of Technology, Pasadena, CA 91125, USA
[7] Laboratoire d'Astrophysique de Marseille (UMR 6110), CNRS-Université de Provence, BP 8, 13376 Marseille Cedex 12, France
[8] NOAO, 950 N. Cherry Ave., Tucson, AZ 85719, USA
[9] Institut d'Astrophysique de Paris, UMR7095 CNRS, Université Pierre et Marie Curie, 98 bis Boulevard Arago, 75014 Paris, France
[10] Max-Planck Institut für Plasmaphysik, Boltzmannstrasse 2, 85748 Garching, Germany
[11] Institute for Astronomy, 2680 Woodlawn Dr., University of Hawaii, Honolulu, HI 96822, USA
[12] LBT Observatory, University of Arizona, 933 N. Cherry Ave., Tucson, AZ 85721, USA
[13] Herzberg Institute of Astrophysics, National Research Council, 5071 West Saanich Road, Victoria, BC V9E 2E7, Canada
Received 2009 October 1; accepted 2009 November 4; published 2009 December 7

ABSTRACT

We present a new analysis of stellar mass functions in the COSMOS field to fainter limits than has been previously probed at $z \leqslant 1$. The increase in dynamic range reveals features in the shape of the stellar mass function that deviate from a single Schechter function. Neither the total nor the red (passive) or blue (star-forming) galaxy stellar mass functions can be well fitted with a single Schechter function once the mass completeness limit of the sample probes below $\sim 3 \times 10^9\,M_\odot$. We observe a dip or plateau at masses $\sim 10^{10}\,M_\odot$, just below the traditional M^*, and an upturn toward a steep faint-end slope of $\alpha \sim -1.7$ at lower mass at all redshifts $\leqslant 1$. This bimodal nature of the mass function is *not* solely a result of the blue/red dichotomy. Indeed, the blue mass function is by itself bimodal at $z \sim 1$. This suggests a new dichotomy in galaxy formation that predates the appearance of the red sequence. We propose two interpretations for this bimodal distribution. If the gas fraction increases toward lower mass, galaxies with $M_{\rm baryon} \sim 10^{10}\,M_\odot$ would shift to lower stellar masses, creating the observed dip. This would indicate a change in star formation efficiency, perhaps linked to supernovae feedback becoming much more efficient below $\sim 10^{10}\,M_\odot$. Therefore, we investigate whether the dip is present in the baryonic (stars+gas) mass function. Alternatively, the dip could be created by an enhancement of the galaxy assembly rate at $\sim 10^{11}\,M_\odot$, a phenomenon that naturally arises if the baryon fraction peaks at $M_{\rm halo} \sim 10^{12}\,M_\odot$. In this scenario, galaxies occupying the bump around M_* would be identified with central galaxies and the second fainter component of the mass function having a steep faint-end slope with satellite galaxies. The low-mass end of the blue and total mass functions exhibit a steeper slope than has been detected in previous work that may increasingly approach the halo mass function value of -2. While the dip feature is apparent in the total mass function at all redshifts, it appears to shift from the blue to the red population, likely as a result of transforming high-mass blue galaxies into red ones. At the same time, we detect a drastic upturn in the number of low-mass red galaxies. Their increase with time seems to reflect a decrease in the number of blue systems and so we tentatively associate them with satellite dwarf (spheroidal) galaxies that have undergone quenching due to environmental processes.

Key words: cosmology: observations – galaxies: evolution – galaxies: luminosity function, mass function – surveys

1. INTRODUCTION

Galaxy formation and evolution is believed to be driven primarily by two processes: firstly, the successive merging of their parent dark matter halos causing accretion of material and ultimately mergers between galaxies; and secondly, the feedback-regulated conversion of gas into stars within galactic disks with subsequent potential rearrangement of the disk material by dynamical processes (secular evolution). Both processes contribute to the growth in stellar mass of galaxies with time. The stellar mass function of galaxies and its evolution with time is therefore fundamental to the understanding of galaxy formation.

The ability to estimate galaxy stellar masses has advanced in recent years in large part because of increasing access to near-IR photometry. Estimates are typically made by fitting multi-band photometry with stellar population synthesis libraries (see, e.g., Brinchmann & Ellis 2000; Bruzual & Charlot 2003; Drory et al. 2004a; Maraston et al. 2006; Marchesini et al. 2009; Conroy et al. 2009), fitting specific spectral features when spectroscopy is available (Kauffmann et al. 2003), or the full spectrum when high-quality spectra are observed (Reichardt et al. 2001; Panter et al. 2004). So far, only the photometric fitting technique has been a viable option for high-redshift surveys. These measurements provide masses with accuracies of ∼0.1–0.3 dex, and systematic uncertainties of up to a factor of 2 depending on the selection and number of photometric bands included and the assumptions made on, among others, the shape of the IMF, the allowed star formation histories (SFHs), the dust extinction model, or the underlying stellar population synthesis method (see, e.g., Drory et al. 2004b; Kannappan & Gawiser

[14] Hubble Fellow

2007; Marchesini et al. 2009; Conroy et al. 2009 for systematic studies on this matter).

Utilizing such techniques, the buildup of the stellar mass density from redshift $z \sim 6$ to the present epoch has been the subject of several studies in the past decade, often relying on deep multi-band imaging surveys in the UV to near-infrared wavelength range (Brinchmann & Ellis 2000; Drory et al. 2001, 2005; Cohen 2002; Dickinson et al. 2003; Fontana et al. 2003; Rudnick et al. 2003, 2006; Glazebrook et al. 2004; Conselice et al. 2005; Chapman et al. 2005; Eyles et al. 2007; Grazian et al. 2007; Stark et al. 2007).

The stellar mass function in the local universe has been measured from large imaging and spectroscopic surveys such as Two-Degree Field (2dF), Sloan Digital Sky Survey (SDSS), and Two Micron All Sky Survey (2MASS; Cole et al. 2001; Bell et al. 2003; Pérez-González et al. 2003; Panter et al. 2004; Baldry et al. 2008). At distances up to $z \sim 1.5$, a number of groups have established a picture of the evolution of the mass function with some detail (Fontana et al. 2004; Bundy et al. 2005, 2006; Borch et al. 2006; Arnouts et al. 2007; Pozzetti et al. 2007; Ilbert et al. 2009b), with generally good agreement between different data sets. To some lesser detail and accuracy, deep surveys have provided data spanning $0 < z \lesssim 5$ (Drory et al. 2005; Conselice et al. 2005; Fontana et al. 2006; Yan et al. 2006; Grazian et al. 2007; Elsner et al. 2008; Pérez-González et al. 2008; Marchesini et al. 2009), and even some estimates at $z \sim 7$ (Bouwens et al. 2006). So far, these high-redshift studies of the stellar mass function emphasized the evolution of galaxies of mass $\log M/M_\odot \gtrsim 10$. Speaking very broadly, the stellar mass density decreases by a factor of 2 to $z \sim 1$, with the most massive galaxies already being in place at earlier epochs. The evolution appears to accelerate quickly beyond $z \sim 1.5$.

In this paper, we concentrate on the low-mass galaxies that have typically been below the completeness limits of previous work at $z > 0.1$. Generally, Schechter (1976) fits to the galaxy stellar mass function with faint-end slope ~ -1.1 to ~ -1.3 have been found adequate to describe the galaxy population (even separated morphologically, by color, or star formation activity; Pannella et al. 2006, 2009; Borch et al. 2006; Arnouts et al. 2007; Ilbert et al. 2009b). Recently, though, a steepening of the slope of the luminosity function below $M_i \sim -17$ in the local universe has been convincingly detected in clusters (Driver et al. 1994; Trentham & Tully 2002; Hilker et al. 2003; Popesso et al. 2005, 2006), groups (Trentham & Tully 2002; Trentham et al. 2005; González et al. 2006), and the field (Blanton et al. 2005). For example, Trentham & Tully (2002) find that the luminosity function in the Virgo cluster, in the NGC 1407 group, and in the Coma 1 group is steep between M_R of -18 and -15 (and flattens again only at $M_R > -15$). Moreover, Baldry et al. (2008) find that the local galaxy stellar mass function steepens as well below $\log M/M_\odot \sim 9.5$ (but also see Li & White 2009).

The steepening of the mass function can also be interpreted as a bimodality: the mass function consists of a sum of (at least) two components. This bimodal behavior has now also been detected at redshifts $z > 0.1$. Pozzetti et al. (2009) find bimodal mass functions to $z \sim 0.5$ from the zCOSMOS spectroscopic survey. They interpret the mass function as being composed of early-type galaxies dominating the massive part and late-type galaxies dominating the less-massive part and contributing the steep faint-end slope. Each of these components is well fitted by a Schechter function. Bolzonella et al. (2009) use the same sample to investigate the bimodality as a function of environment. They find that at $z \lesssim 0.5$, the shape of the galaxy stellar mass function in high- and low-density environments become markedly different, with high density regions showing a stronger bimodality.

We extend the study of the shape of the galaxy stellar mass function, particularly at low masses, to $z \sim 1$, with stellar mass limits $\sim$1.5 dex lower than can be achieved with spectroscopic studies. We investigate actively star-forming galaxies and passively evolving galaxies separately; we study how the change in slope may be caused by the presence of multiple galaxy populations, that taken together, lead to a mass function shape that is more complex than a single power law with an exponential cutoff or even a simple combination of early- and late-type components. We show that the blue mass function itself is bimodal and that passive galaxies exhibit a faint-end upturn, likely caused by dwarf spheroidal galaxies linked to the faint end of the blue galaxy population.

This paper is organized as follows. In Section 2, we introduce the galaxy sample that we use in this work. In Section 3, we discuss the stellar population models used to derive stellar masses and the resulting mass completeness limits. In Section 4, we present the stellar mass function of active and passive galaxies; and we discuss our results in Section 5. Finally, we summarize this work in Section 6.

Throughout this work we assume $\Omega_M = 0.3$, $\Omega_\Lambda = 0.7$, and $H_0 = 70\,h_{70}^{-1}$ km s^{-1} Mpc^{-1}. Magnitudes are in the AB system. We will denote galaxy stellar masses by the symbol M—or M_g where an explicit distinction form halo masses, denoted by M_h, is necessary. The symbol M^* is reserved for the characteristic mass parameter of the Schechter function.

2. SAMPLE SELECTION

The primary focus of this paper is determining the abundance of low-mass galaxies and characterizing the shape of the mass function, especially at the low-mass end. These galaxies are faint by definition, with $i \gtrsim 23$ and $K \gtrsim 23$, sources that are typically beyond the range of magnitude-limited spectroscopic surveys like DEEP2, VVDS, or zCOSMOS (Davis et al. 2003; Le Fèvre et al. 2005; Lilly et al. 2007). As such, we must rely on photometric redshifts.

We use the COSMOS catalog with photometric redshifts derived from 30 broad and medium bands described in Ilbert et al. (2009a) and Capak et al. (2007), version 1.5, dated 2008 April 5. We restrict ourselves to objects with $i^+_{\rm AB} < 25$. At this limit, the rms photo-z accuracy at $z < 1$ is $\sim$0.03 in $\Delta z/(1+z)$ (Figure 9 in Ilbert et al. 2009a). At $z > 1$, the quality of the photometric redshifts quickly deteriorates. The detection completeness at $i^+_{\rm AB} = 25$ is >90% (Capak et al. 2007). Additionally, we require a detection in the Ks band (McCracken et al. 2009) to ensure that the stellar mass estimates at the faint end are still reliable, thus we add the constraint $Ks < 24$. The surface brightness sensitivity limit for the i^+ data is 28.4 mag arcsec^{-1} at 5σ. At this limit, an object of 25th magnitude would have to be 5.″4 across (with no bulge) to have a chance of being missed. At 23rd magnitude that number increases to 7″. It is hence very unlikely that surface brightness is the dominant selection effect at low luminosities where galaxies are very compact (in contrast to the situation in local-universe surveys; see simulations in Capak et al. 2007).

To ensure high-quality photometric redshifts, we will limit the redshift range to $z < 1$ and to sample enough volume to $z > 0.2$. We have made sure that our results are not sensitive

to this selection through repetition of our analysis with relaxed magnitude limits. Our mass functions change neither shape nor their faint-end slope, if we drop the Ks-band selection and push the i^+ selection to 26th magnitude. Dropping the Ks-band selection leads to a gain in about one bin in depth (0.25 dex in mass), albeit with increased stellar mass errors by about 20% on individual sources below the Ks-band limit, but no change in the faint-end slope (the z- and the J band still provide enough information on the NIR light). Nor do our results change if we impose a brighter selection cut of $i^+_{AB} < 24$, apart from a restriction in redshift range.

We use the photometric data in the u^* (CFHT), B_J, V_J, g^+, r^+, i^+, z^+ (Subaru), J (UKIRT), and Ks (CFHT) bands for our analysis, totaling nine bands. We explicitly exclude the IRAC1-channel data (3.6 μm) due to their confusion-limited nature at $m_{\rm AB} = 24$, which would otherwise restrict the analysis to brighter magnitudes than is possible with the Ks-band data. This is in contrast to the mass function analysis by Ilbert et al. (2009b), who use an IRAC1-selected catalog. However, we have verified that adding the IRAC1 data where available does not alter the stellar masses significantly and our mass functions are consistent in the overlapping mass range with the ones derived by Ilbert et al. (2009b) including the IRAC1 channel. In a similar analysis, Fontana et al. (2006) find that including IRAC1–IRAC4 at $z \lesssim 1$ data does reduce the uncertainties in the mass estimate somewhat, but does not change the masses systematically (Figure 1 in their paper). The reason for this is that in the redshift range of interest here ($z \lesssim 1$), the rest frame near-IR light is sampled well enough by the J and Ks data, so that the addition of IRAC1 data does not add much information about the presence of an old stellar population.

In addition to the above magnitude limits, we require that a photometric redshift be assigned to the objects and that the object not be in a masked image region (e.g., near bright stars, image border, and detector defects) in any of the B_J, V_J, i^+, and z^+ bands. The total area of the survey we use after masking is 1.73 deg^2.

We use two methods to remove stars from the sample. First, sources where the best-fitting stellar spectral energy distribution (SED) template has a lower χ^2 than the best-fitting galaxy SED template are discarded. This method is discussed and shown to be very reliable at $i^+ < 24$ mag (Ilbert et al. 2009a; 2% of the total population at $i^+ < 24$ could be stars not recognized by the SED classifier while only 0.2% of extended sources in the ACS data are classified as stars by the χ^2-criterion). In addition, we remove sources with point-like ACS morphologies using the catalog presented in Leauthaud et al. (2007). This ACS cut removes an additional 1%–3% of the total number of sources and is especially important among passive galaxies at $z > 0.6$. We also note that ~15% of point-like sources in the COSMOS field are found to be galaxies, however, Robin et al. (2007) show that these are faint high-z objects that will not affect our analysis.

Our final sample contains 138001 sources in the redshift range $0.2 < z < 1$. We will divide this redshift range into four equally spaced bins in the following analysis. Table 1 lists the number of sources in our final sample and its subsamples as well as the volume probed by each redshift bin.

Table 1
Sample Size

$z_{\rm min}$	$z_{\rm max}$	Volume	Number of Galaxies		
		(10^6 Mpc^3)	Active	Passive	Total
0.2	0.4	0.56	27,931	3553	31,484
0.4	0.6	1.23	27,258	2289	29,547
0.6	0.8	1.92	34,298	2587	36,885
0.8	1.0	2.53	37,131	2954	40,085

2.1. Reliability of the Photometric Redshifts

While our mass functions yield consistently steep faint-end slopes in all of the redshift bins studied, the lowest redshift bin provides the deepest probe of the low-mass galaxy population and our strongest constraints at this mass range. A top concern, therefore, is that distant galaxies with much larger redshifts may have been mistakenly shifted to the $0.2 < z < 0.4$ bin and, with faint apparent magnitudes, assigned masses with $\log M/M_\odot < 9$. Indeed, photo-z estimates often suffer from degeneracies between the 4000 Å break at $z \sim 0.2$ and the Lyman break at $z \sim 4$, especially if U-band or near-IR photometry is shallow or missing. We largely mitigate these problems by requiring detections for all sources in i^+ and Ks in addition to implementing our magnitude limits to reject noise and false detections. We confirm this by verifying that our results do not change if we reject all sources which show a second peak in their redshift probability distribution with amplitude larger than 5%. We note that Ilbert et al. (2009a) find no evidence of redshift degeneracies or persistent catastrophic outliers in the COSMOS photo-z catalog at our magnitude limits that could threaten the robustness of our result.

Beyond the photometry requirements, we have searched the NUV–R–J color–color diagram for sources with unusual colors that could indicate a contaminating population. This is illustrated in Figure 1. Given the mass completeness limit estimate for each redshift bin, $M_{{\rm lim},i}$, we highlight in blue those galaxies with $M < 3 \times M_{\rm lim}$. These represent the lowest masses at which the star-forming sample is still complete. In large part, they follow the locus of star-forming galaxies. No outlier population is apparent. We have also repeated this experiment for galaxies whose photo-z uncertainties are particularly large (a 68% confidence interval larger than 0.5 in redshift) and again find no evidence of contamination. Finally, we use Monte Carlo simulations described in more detail below to convince ourselves that the mass function is sufficiently robust against the errors in the photometric redshifts.

2.2. Separating Star-forming from Passive Populations

The low-mass galaxies contributing to the steep faint-end slope of the mass function are too faint to be morphologically classified using the available *Hubble Space Telescope* (*HST*) data. Instead, we turn to their colors and SEDs to shed light on their properties. Motivated by the ability to break degeneracies between age and dust, we use a UV–optical–IR (NUV–R–J) color–color diagram to study our sample, finding that the best-fitting SED templates returned by the photo-z code do a good job of distinguishing star-forming from passive galaxies. We group together SED types 1–8 from the COSMOS photo-z catalog as "SED early-types" (see Ilbert et al. 2009a and Polletta et al. 2007 for details on the SED templates) and highlight them in red in Figure 1. At most redshifts, the early-type SED designation overlaps well with the associated clump of passive galaxies identified with red NUV–R colors and blue R–J colors (see Williams et al. 2009 and Ilbert et al. 2009a). A joint color cut indicated by the two lines would select additional passive systems that are not selected by the SED classification. At $z \lesssim 0.6$, the color cuts select ~10% more passive galaxies, many of these systems scattered between

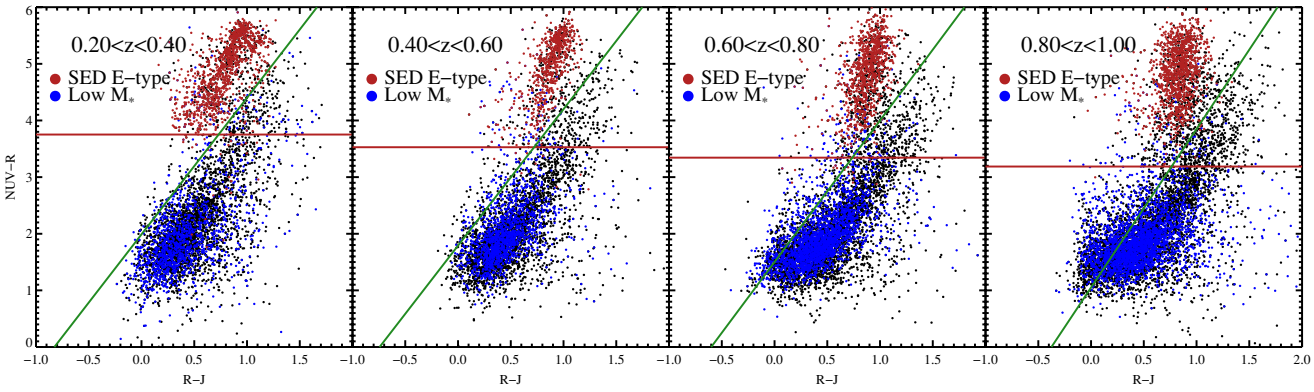

Figure 1. Comparison of the selection techniques of passive galaxies in the NUV$-r$ vs. $r-J$ color–color plane. Galaxies identified as passive by SED fitting are marked as red points. The lines show the color cuts defined by Williams et al. (2009) for identifying passive systems. In addition, galaxies with masses between the mass limit and three times the mass limit in each redshift bin are marked in blue, to look for low-mass galaxies with unusual colors which would indicate a possible problem with the photometric redshifts.

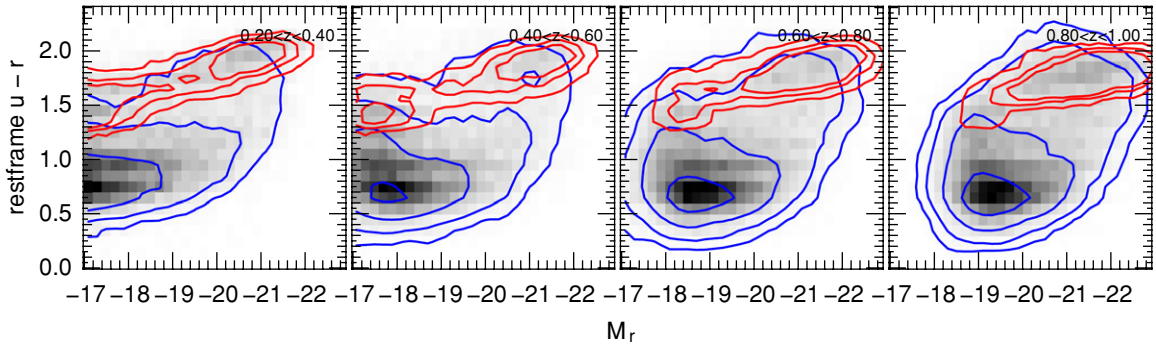

Figure 2. Distribution of galaxies in our sample in the absolute magnitude, M_r, vs. $u-r$ rest-frame color plane. The gray-scale shading marks the density of all objects in this plane, while the blue and red contours outline the distributions of the blue (active) and red (passive) subsamples, respectively.

star-forming and passive sequences. At $z \sim 1$, however, the SED method identifies as many as 15% fewer galaxies in the passive clump.

With none of these classifiers being demonstrably preferable, we choose to proceed with the SED-based classification. We have re-analyzed the data with the NUV–*R*–*J*-based classification, and find that the results are fully consistent. In particular, this excludes that the mass function of faint red galaxies is distorted significantly by some faint blue galaxies (which are more numerous by a factor >10) being misidentified as red galaxies by one of these classification methods but not the other. Also, if misclassified blue galaxies were (partly) responsible for the faint red population, we would expect this population to become more numerous at high z where signal-to-noise ratio (S/N) is lower. This turns out not to be the case (see below).

In Figure 2, we show the distribution of the galaxies in our sample in the absolute magnitude, M_r, versus $u-r$ rest-frame color plane. The gray-scale shading marks the density of all objects in this plane, while the blue and red contours outline the distributions of the blue and red subsamples, respectively.

3. DERIVING STELLAR MASSES

Stellar masses (the mass locked up in stars) are routinely derived by comparing multi-band photometry to a grid of stellar population models of varying SFHs, ages, and dust content. We follow the same approach in this work. Our procedure is described in detail and compared against spectroscopic and dynamical mass estimates in Drory et al. (2004b); although in the present work, we will explore a wider set of stellar population models described in the following paragraphs.

3.1. Stellar Population Models

We allow for SFHs consisting of two components: a main population of stars formed in a smooth SFH and a modulation by a second population formed in a burst of star formation just prior to observation. The main component is parameterized by a SFH of the form $\psi(t) \propto \exp(-t/\tau)$, with $\tau \in [0.5, \infty]$ Gyr and a metallicity of $-0.6 < [\mathrm{Fe/H}] < 0.3$. The age, t, (defined as the time since the onset of star formation) is allowed to vary between 0.5 Gyr and the age of the universe at the object's redshift. We linearly combine this with a starburst modeled as a 100 Myr-old constant star formation rate (SFR) episode of solar metallicity. We restrict the burst fraction, β, to the range $0 < \beta < 0.15$ in mass. Higher values of β are degenerate and unnecessary since such SEDs are covered by models with a young main component. We adopt a Chabrier (2003) initial mass function (IMF) truncated at 0.1 $M_\odot$ and 100 $M_\odot$ for both components. This choice of IMF is described by a power law at $M \geqslant 1$ $M_\odot$ and a lognormal distribution below. The Chabrier IMF yields masses lower by about 0.25 dex compared to a Salpeter (1955) single-slope IMF of the form $dn/dm \propto m^{-2.35}$. We use the stellar population synthesis codes of Bruzual & Charlot (2003, BC03) and the BC03 models updated in 2007[15] with an improved treatment of thermally pulsing asymptotic giant branch (TP-AGB) stars, hereafter referred to as BC07 models.

Additionally, both components are allowed to exhibit a different and variable amount of extinction by dust. We assume a Calzetti et al. (2000) form for the extinction law. This takes into account the fact that young stars are found in dusty environments

[15] Often referenced as S. Charlot & G. Bruzual (2007, in preparation).

and that the starlight from the galaxy as a whole may be reddened by a (geometry dependent) different amount. In fact, Stasińska et al. (2004) find that the Balmer decrement in the SDSS sample is independent of inclination, which, on the other hand, is driving global extinction (see, e.g., Tully et al. 1998). We verified that using the Milky Way extinction law or the SMC extinction law instead does not change our conclusions. This is due to our restricted redshift range which means we do not probe too far into the rest-frame UV where the different slopes of the extinction laws matter most and because low-mass galaxies at $z < 1$ are not heavily obscured, unlike galaxies of the same mass at $z \gtrsim 2$.

We compute the full likelihood distribution on a grid in this six-dimensional parameter space (τ, [Fe/H], t, A_V^1, β, A_V^2), the likelihood of each model being $\propto \exp(-\chi^2/2)$. To compute the likelihood distribution of mass-to-light ratio (M/L), we weight the M/L of each model by its likelihood and marginalize over the stellar population parameters. The uncertainty in M/L is obtained from the width of this distribution, which falls between ± 0.1 and ± 0.3 dex at 68% confidence level on average. The uncertainty has a weak dependence on mass (increasing with lower S/N photometry), and much of the variation is in spectral type: early-type galaxies have more tightly constrained masses than late types.

We have also compared the masses obtained with this code to the ones obtained with the code employed by Bundy et al. (2006) and the Bruzual & Charlot (2003) stellar population synthesis models. We find that the masses computed by both codes are consistent and show no trends with luminosity or redshift. Hence, the stellar masses are not sensitive to the particular choice of grid parameters and fitting procedure (within reasonable limits, of course).

Of much graver concern than errors stemming from uncertainties in the photometry are systematic problems with the stellar population libraries and the implicit priors on evolutionary histories introduced by the finite model grid. For a comprehensive analysis see Marchesini et al. (2009). One of the main issues is the treatment of the TP-AGB stars, whose light dominates in intermediate-age (0.5–2 Gyr) populations from the I band through the near-IR (Maraston 2005; Maraston et al. 2006). The contribution of these stars can lead to changes of up to a factor of 2–3 in the stellar mass estimates for extreme cases (however, these are unlikely to be observed at $0 < z < 1$) and if the relevant wavelength range is poorly covered by the data. TP-AGB spectral signatures are strongest at $\sim$1 μm rest frame, which is always within the observed-frame colors in our data set. Nevertheless, we base our model grid on the BC03 models as well as on the BC07 models, which incorporate an improved prescription for the treatment of the TP-AGB phase (also see Bruzual 2007).

Despite the problems with late stellar evolutionary phases, Conroy et al. (2009) in a thorough investigation of population synthesis modeling, argue that the M/Ls are largely resistant to the uncertain contribution from TP-AGB stars as well as other limitations in the models. We will nevertheless compare stellar masses based on both evolutionary synthesis codes to make sure our results do not depend on a specific choice of a stellar population model.

3.2. Mass Completeness Limits

Determining the selection function in stellar mass for a flux-limited sample is not possible in a rigorous way: knowledge of the intrinsic frequency distribution of M/Ls of the galaxy population *above and below* the flux limit is necessary, but generally not available. Several methods to (conservatively) *estimate* the completeness limit have been employed. Most commonly and simplistically, one assumes that a maximally old population (and hence with maximally high M/L in the absence of dust) at the flux limit of the survey will yield a conservative upper limit to the mass that potentially could be affected by incompleteness (e.g., Drory et al. 2005; Fontana et al. 2006; Borch et al. 2006; Bundy et al. 2006; Pérez-González et al. 2008).

Marchesini et al. (2009) employed a different approach: they use successively deeper data sets to empirically determine their mass completeness function at shallower flux limits. This approach, while clearly better than the maximum-M/L method is not feasible for large, uniformly deep surveys such as COSMOS (there are no significantly deeper data sets observed in the same passbands). However, it is possible in a limited way using smaller pencil-beam surveys and we will do so as a sanity check.

We wish to separate our sample into blue, star-forming galaxies and red, quiescent ones. It is therefore also necessary to determine separate completeness limits for both populations. We will refrain from attempting to correct for incompleteness. Instead, we conservatively estimate the point from which incompleteness may significantly affect our sample and limit ourselves to masses larger than this number. For the red population, a maximal M/L approach seems sufficient. At the redshifts of interest ($0 < z < 1$), this population consists of ellipticals and quiescent spirals with little evolution in number density with masses $\log M/M_\odot \gtrsim 10$ (Bell et al. 2004; Bundy et al. 2005; Pozzetti et al. 2007; Pérez-González et al. 2008; Ilbert et al. 2009b; Williams et al. 2009). Stronger evolution and dust-extincted starbursts appear in large numbers at $z \gtrsim 1.5$ (Fontana et al. 2006; Daddi et al. 2007; Pérez-González et al. 2008; Ilbert et al. 2009b). In the local universe, most low-mass passive galaxies are dwarf spheroidals, which are very unlikely to contain significant amounts of dust. We obtain an estimate for the completeness limit of our sample at $i^+ < 25$ and $Ks < 24$ of $\log M/M_\odot = 9$ at $z = 0.3$ and $\log M/M_\odot = 10.1$ at $z = 0.9$.

Blue star-forming galaxies have much more varied M/L values. However, the largest variation is in $\sim L^*$ spirals, with a large contribution to this variation coming from variable dust extinction; blue objects fainter than $M_r \sim -20$ at $z \sim 0$ have much more uniform properties (Kauffmann et al. 2003) and in generally much lower amounts of dust ($A_{\mathrm{H}\alpha} < 1$ mag at $\log M/M_\odot < 9$ compared to $A_{\mathrm{H}\alpha} \sim 2 \pm 1.5$ at $\log M/M_\odot > 10$; Brinchmann et al. 2004). In accordance with the conclusions reached by Kauffmann et al. (2003) in the local universe, the M/Ls at magnitudes fainter than $M_r \sim -20$ become roughly independent of magnitude, converging to $M/L_r \sim 1$. At brighter magnitudes than $M_r \sim -20$, M/L_r rapidly increases with luminosity.

We can therefore assume that models with $M/L_r \sim 1$ resemble the faint galaxy population and a limiting mass computed using a range of models with values of M/L_r close to or above 1 will yield a sufficiently robust limit. Using plausible numbers for a rather extreme model of a low-mass galaxy with a (light-weighted) age of 1–2 Gyr, star formation timescale (τ = 5–10 Gyr), and the maximum dust extinction found in the local universe for such objects ($A_{\mathrm{H}\alpha} = 1$ mag), therefore pushing M/L to the high side of the distribution, we obtain completeness limits roughly 0.4–0.7 dex lower in mass than

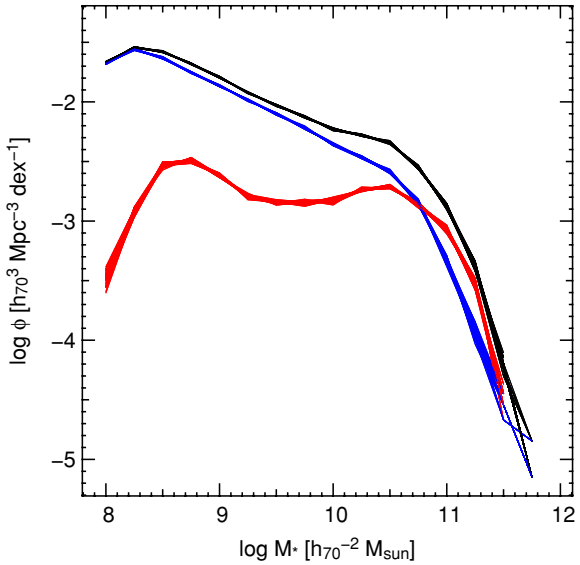

Figure 3. Monte Carlo realizations of the stellar mass function to explore the influence of the uncertainties in the photometric redshifts on the shape of the stellar mass function. The mass function of passive galaxies is marked in red, that of star-forming galaxies in blue, and that of all galaxies in black. Each line corresponds to one realization where the redshifts have been randomly drawn for each object individually from the 95% confidence region of the redshift probability distribution.

Table 2
Mass Completeness Limits

$z_{\rm min}$	$z_{\rm max}$	Active $\log M_{\rm lim}/M_\odot$	Passive $\log M_{\rm lim}/M_\odot$
0.2	0.4	8.3	8.9
0.4	0.6	8.9	9.2
0.6	0.8	9.2	9.8
0.8	1.0	9.4	10.1

for the red galaxies. We can verify these limits using the much smaller but deeper FORS Deep Field (FDF) data (Drory et al. 2005). Comparing the COSMOS mass function at $0.4 < z < 0.6$ with the FDF mass function bin $0.25 < z < 0.75$ from Drory et al. (2005), we see that the point where the COSMOS data start to fall below the FDF data coincides with the mass limit for the blue population as estimated here (see Figure 5 below). The completeness limits are summarized in Table 2.

4. THE GALAXY STELLAR MASS FUNCTION

We compute the galaxy stellar mass function using the $V_{\rm max}$ method to account for the fact that fainter galaxies may not be detectable throughout a whole redshift bin. Hence, each galaxy in a given redshift bin contributes to the number density an amount inversely proportional to the fractional volume of the bin in which the galaxy would be visible. Given the conservative mass completeness limits applied in our analysis, we find that the $V_{\rm max}$-corrections to the mass function data points above the mass limit are negligible (below 5% in all bins). Therefore, the data used in the analysis of the mass function are essentially free of incompleteness corrections.

4.1. Uncertainties Due to Photometric Redshifts

Aside from the potential for catastrophic failures (discussed in Section 2.1), the use of photometric redshifts implies imprecise distances and therefore imprecise absolute magnitudes or

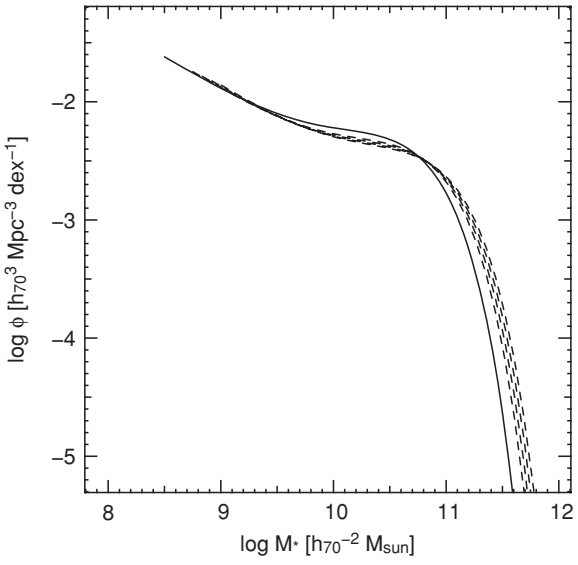

Figure 4. $z \sim 0$ galaxy stellar mass function from SDSS data (Baldry et al. 2008; solid line) convolved with the mass error distribution due to the use of photometric redshift based distances (dashed lines) at $z \in \{0.3, 0.5, 0.7, 0.9\}$.

stellar masses. On the exponential part of the mass function, uncertainties in the distance will scatter objects preferentially from lower masses (where objects are exponentially more abundant) to higher masses. It may also introduce a systematic effect on the faint-end slope.

We investigate the effect of uncertainties in the photometric redshifts on the mass function by means of Monte Carlo simulations. We re-assign redshifts to each object drawing from the redshift probability distribution in the 95% confidence region around the main peak. We take the asymmetry of the redshift probability distribution into account by using different confidence limits for the region below and above the main peak. We then recompute stellar masses with such new redshifts and redetermine the mass function. In Figure 3, we plot 50 realizations of mass functions obtained from these simulations. We conclude that redshift errors do not add large uncertainties at the faint end. The uncertainties in each mass bin at $\log M/M_\odot \leqslant 10.5$ we derive from these simulations are $\lesssim$0.03 dex for the blue and total mass functions, and $\lesssim$0.05 dex for the red mass function. The inferred faint-end slopes agree to within a fraction of the formal fit uncertainty on the slope parameter.

The slope may still change systematically, though. To test this, we run another set of simulations, this time using only objects with small redshift errors (the best 20% of the $\Delta z/(1+z)$ distribution) and increase their errors by a factor of 2 and 3. In neither case is the slope significantly altered compared to the one obtained with the original small redshift errors (the objects in these simulations are obviously not quite as faint as those in the whole sample, but faint enough below M^* to securely measure a change in slope).

However, as expected, there is an effect on the bright end of the mass function. Figure 4 shows the $z \sim 0$ SDSS mass function by Baldry et al. (2008) and the result of convolving it with our mass error distributions. The presence of mass uncertainties leads to a significant overestimate of the mass function at the high-mass end. In summary, we conclude that redshift uncertainties do not influence the faint-end slope of the mass function systematically but do add a small random uncertainty. At the bright end, they lead to larger uncertainties and a systematic "brightening" of the exponential cutoff. We

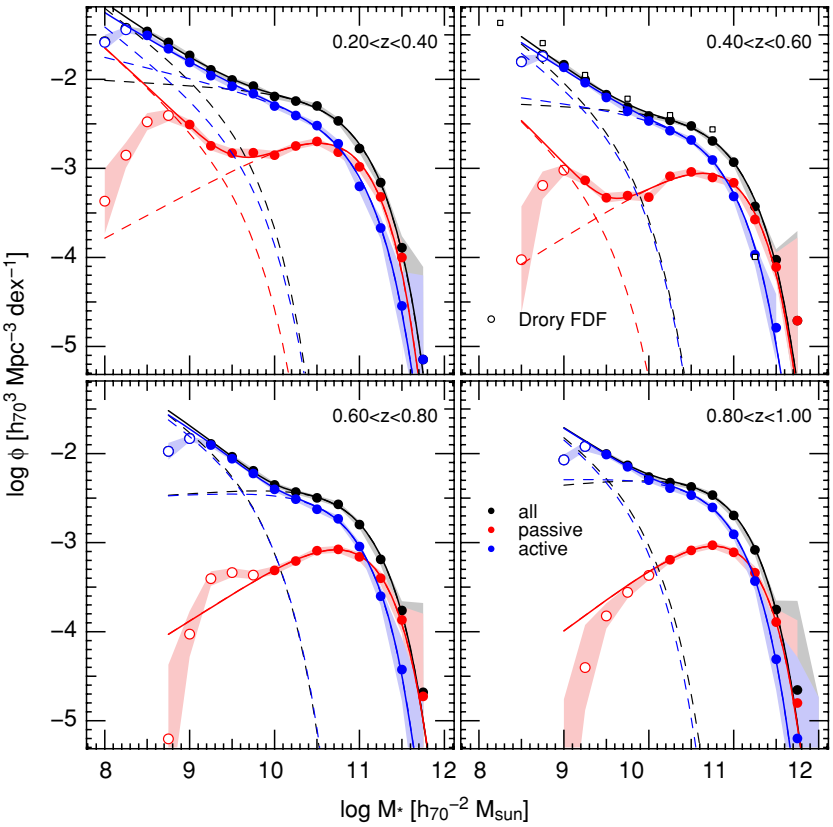

Figure 5. Stellar mass function of galaxies in four redshift bins in the interval $0.2 < z < 1.0$. The mass function of passive galaxies is marked in red, that of star-forming galaxies in blue, and that of all galaxies in black. Data points below the mass completeness limits are denoted by colored open symbols. The uncertainty in the mass function due to Poissonian errors in the counts as well as the uncertainty propagated through photometric redshifts (see the text) is shown as shaded regions. Data from the FORS Deep Field (Drory et al. 2005) are shown as small black open squares at $z = 0.5$ for comparison. The solid lines show double Schechter function fits to the data (Equation (1)). The thin dashed lines show the individual bright and faint components of the double Schechter functions.

will add the uncertainties from these simulations (the scatter seen in Figure 3) to the total uncertainties in our mass functions.

4.2. Characterizing the Shape of the Mass Function

We plot the galaxy stellar mass function in Figure 5. The mass function of passive galaxies is shown in red, that of active galaxies in blue, and that of all galaxies in black. Filled symbols mark data points above the formal completeness limit, open symbols data below the completeness limit and hence where number densities are likely to be artificially low.

It is evident from Figure 5 that a single Schechter function would not be a good fit to the total mass function (black points) or to the active galaxy mass function (blue points) at any redshift $z \leqslant 1$. At $z \leqslant 0.5$, the passive galaxy mass function clearly shows a marked paucity of objects at intermediate mass and a sharp upturn at low mass. At $z \sim 0.7$, the upturn in the passive galaxy mass function is still detected, however the mass function is no longer complete at any point that deviates upward, and at $z \sim 0.9$ we are unable to detect an upturn. At these two redshift bins, using only data above the completeness limit, the passive galaxy data are adequately fit by a single Schechter function.

One way to describe the mass function shape is as a sum of (at least) two components, that is, a bimodal distribution. Double Schechter functions (the sum of two Schechter functions, sometimes sharing a common normalization, ϕ^*, characteristic scale, M^*, or both) have been used by other authors to fit the luminosity or mass functions with steepening faint-end parts (Driver et al. 1994; Popesso et al. 2006; Baldry et al. 2008; Pozzetti et al. 2009). These work well to describe the total population and the active sub-population in our data set. However, more flexibility is needed to model the transition region between bright and faint populations in the passive sub-population at $z < 0.6$, as these functions fail to reproduce the fairly wide dip in the data. We, therefore, opt to fit all mass functions by a sum of two Schechter functions without restricting the parameters further:

$$\begin{aligned}\phi(M)dM &= \phi_{\rm b}(M)dM + \phi_f(M)dM \\ &= \phi^*_{\rm b}\left(\frac{M}{M^*_{\rm b}}\right)^{\alpha_{\rm b}} \exp\left(-\frac{M}{M^*_{\rm b}}\right) dM \\ &\quad + \phi^*_f\left(\frac{M}{M^*_f}\right)^{\alpha_f} \exp\left(-\frac{M}{M^*_f}\right) dM. \end{aligned} \quad (1)$$

We define $M^*_{\rm b}$ and M^*_f such that $M^*_{\rm b} > M^*_f$ thereby identifying the first term, $\phi_{\rm b}(M)$, with a population of bright galaxies and the second term, $\phi_f(M)$, with a population of faint galaxies.

The results of fitting Equation (1) to the data are shown in Figure 5. Solid lines mark the fit, $\phi(M)$, to the active, passive, and total mass functions while the dashed lines show the individual components, $\phi_{\rm b}(M)$ and $\phi_f(M)$, of each fit. We again use blue for the active galaxies, red for the passive galaxies, and black for the total population. The best-fit parameters of Equation (1) are listed in Table 3. The table also lists the reduced χ^2 values for the best fit, as well as the χ^2 obtained by fitting only a single Schechter function to the data instead of Equation (1). The reduced χ^2 values are between 1 and 2. The best χ^2 values obtained with a single Schechter function are between 7 and

Table 3
Double Schechter Fit Parameters to the Mass Function

z		ϕ_b^* ($10^{-3}\,h_{70}^3$ Mpc^{-3} dex^{-1})	$\log M_b^*$ ($h_{70}^{-2}\,M_\odot$)	α_b	ϕ_f^* ($10^{-3}\,h_{70}^3$ Mpc^{-3} dex^{-1})	$\log M_f^*$ ($h_{70}^{-2}\,M_\odot$)	α_f	χ^2	$\chi^2_{\rm single}$ [a]
0.2...0.4	All	2.89 ± 0.23	10.90 ± 0.11	-1.06 ± 0.03	1.80 ± 0.29	9.63 ± 0.09	-1.73 ± 0.09	1.9	13.0
	Passive	1.96 ± 0.12	10.80 ± 0.99	-0.49 ± 0.14	0.49 ± 0.12	9.54 ± 0.09	-1.85 ± 0.20	1.8	16.8
	Active	1.66 ± 0.10	10.83 ± 0.10	-1.23 ± 0.03	0.98 ± 0.23	9.66 ± 0.10	-1.75 ± 0.12	1.8	7.0
0.4...0.6	All	1.74 ± 0.09	10.91 ± 0.11	-1.05 ± 0.02	1.43 ± 0.23	9.70 ± 0.10	-1.76 ± 0.16	1.6	13.6
	Passive	0.95 ± 0.09	10.85 ± 0.11	-0.40 ± 0.06	0.28 ± 0.03	9.41 ± 0.19	-1.84 ± 0.29	1.6	12.7
	Active	1.38 ± 0.06	10.76 ± 0.11	-1.13 ± 0.05	1.29 ± 0.04	9.69 ± 0.09	-1.71 ± 0.19	1.3	9.6
0.6...0.8	All	2.16 ± 0.13	10.95 ± 0.10	-0.93 ± 0.04	2.89 ± 0.26	9.75 ± 0.10	-1.65 ± 0.08	1.5	11.9
	Passive	0.90 ± 0.05	10.94 ± 0.09	-0.39 ± 0.05	...	...	...	...	0.7
	Active	1.86 ± 0.11	10.80 ± 0.10	-0.95 ± 0.04	2.78 ± 0.31	9.75 ± 0.10	-1.61 ± 0.11	1.6	9.1
0.8...1.0	All	2.94 ± 0.13	10.92 ± 0.10	-0.91 ± 0.03	2.12 ± 0.29	9.85 ± 0.10	-1.65 ± 0.24	1.4	9.1
	Passive	1.03 ± 0.05	10.91 ± 0.11	-0.29 ± 0.04	...	...	...	...	0.3
	Active	2.51 ± 0.10	10.81 ± 0.11	-0.97 ± 0.03	2.16 ± 0.37	9.80 ± 0.10	-1.66 ± 0.36	1.4	8.0

Note. [a] Reduced χ^2 for a fit with a single Schechter function.

13, confirming that a single Schechter function indeed does not provide satisfactory fits with high significance.

We find a faint-end slope significantly steeper than previous studies, $\alpha_f \sim -1.7 \pm 0.15$ with very little variation with redshift and between the blue, red, and total samples. With shallower mass limits, slopes typically around $\alpha \sim -1.2$ are found (e.g., Bell & de Jong 2001; Cole et al. 2001; Drory et al. 2004a; Fontana et al. 2004, 2006; Ilbert et al. 2009b, although evidence for a steeper slope has been put forward, for example, by Drory & Alvarez 2008) from comparing the evolution of the mass function to the expectation from SFRs. The value we find at $z = 0.3$, $\alpha_f \sim -1.7 \pm 0.1$, is consistent with that of Baldry et al. (2008) in the SDSS, who find a best-fit value of $\alpha_2 = -1.58 \pm 0.02$, with $\alpha_2 = -1.8$ providing equally good fits given the non-negligible role of systematic surface brightness selection effects at their faint end. We find that the faint-end slope of the blue and the red population at $z = 0.3$ and $z = 0.5$, where both can be measured, are remarkably similar. The red faint-end slope is formally steeper by 0.1, but with a large uncertainty of 0.2–0.3 (evidence for an excess of red dwarf galaxies was recently also found by Salimbeni et al. 2008 in the GOODS data). We do not detect a significant trend of the faint-end slope of the blue population and hence of the total mass function with redshift up to $z = 1$.

The characteristic mass of the faint blue sub-component shows a slight increase with redshift, from $\log M_f^* \sim 9.6$ at $z = 0.3$ to $\log M_f^* \sim 9.8$ at $z = 0.9$ (significant at the 2σ level), while the characteristic mass in the bright component, M_b^* does not show evolution in this data set.

Surveys of 1–2 deg^2 based on single fields can suffer from significant cosmic variance uncertainties. The volume probed by our redshift bins lies between $0.56 \times 10^6 h_{70}^{-3}$ Mpc^3 and $2.53 \times 10^6\ h_{70}^{-3}$ Mpc^3 (equivalent to box sizes between $82\ h_{70}^{-1}$ Mpc and $136\ h_{70}^{-1}$ Mpc; see Table 1). Cosmic variance on such scales is mostly thought to affect the overall normalization of the mass function, although possibly the shape as well (Stringer et al. 2009). In the COSMOS data, we notice a strong underdensity at $z \sim 0.5$, as has been seen before (also see Meneux et al. 2009), with the characteristic density, ϕ^*, being about a factor of 2 lower (more so in the red population than in the blue). Looking at the distribution of spectroscopic redshifts from zCOSMOS (Figure 8 in Lilly et al. 2009), it is evident that over the interval $0.4 < z < 0.65$ there is a marked paucity of dense structures compared to lower and higher redshifts, which confirms our above observation. The comparison with the spectroscopic zCOSMOS sample also excludes the possibility that the density structure in the field is caused by systematic failures of the photometric redshifts. This variance in average density influences our ability to make statements on redshift evolution significantly. Despite the large cosmic variance, we do see a shift from blue to red galaxies at the bright end as redshift decreases.

A word of caution is warranted at this point; Equation (1) is by no means the only possible fitting function able to reproduce the data in a statistically satisfactory way. For instance, a faint component with a sharper than exponential cutoff works just as well. Also, the bright part of the (red galaxy) mass function can be fit by a symmetrically peaked function, similar to a Gaussian. Thus, one should not base any interpretations solely on the particular fitting function chosen. We emphasize that the fitting functions in the overlap region between the bright and faint mass functions should not be taken to be more than descriptions of the data. Without classifying objects individually as belonging to the bright or faint sub-population, the transition region between the two can be fit in many ways and the particular representation chosen here should not be assigned physical meaning.

4.3. Effects of Stellar Population Models

Can the features of interest in the stellar mass function be explained as artifacts introduced by the adopted stellar population models? First, we test whether TP-AGB stars can influence the faint-end slope of the blue star-forming mass function. We recompute the mass function using a stellar population grid based on the BC07 models, keeping all other model grid parameters identical (see Section 3.1). Figure 6 shows the difference in the mass function obtained with the BC03 models (Figure 5) and the mass function obtained with the BC07 models. We do not find significant systematic differences in the mass function of passive galaxies. In contrast, systematic differences are small but noticeable in the active population and they increase with redshift. As expected, the stellar masses obtained with the BC07 models are smaller than the ones obtained with the BC03 models (Maraston 2005; Maraston et al. 2006; Bruzual 2007). The difference is negligible at $z \sim 0.3$. Beyond $z \sim 0.5$, the difference exceeds the uncertainties in the masses over much of the mass range, increasing at masses above and below $10^{10}\ M_\odot$ to a maximum of 0.1 to 0.15 dex. However,

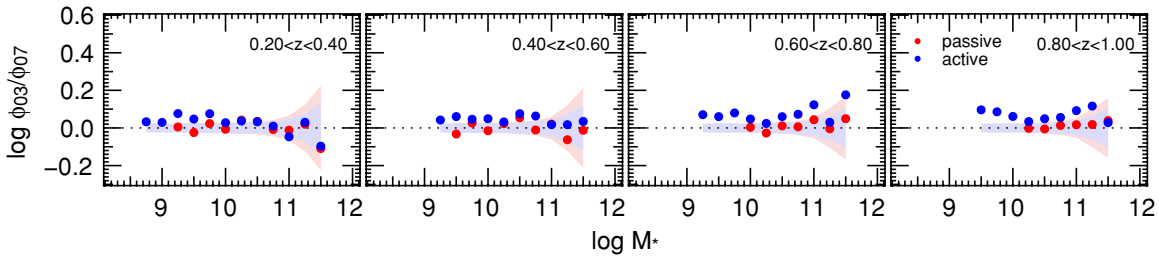

Figure 6. Ratio of the galaxy stellar mass function computed with stellar population synthesis models based on the BC03 code and the BC07 code, which includes a refined treatment of the post-AGB stellar evolutionary phases. The values for active and passive galaxies are marked by blue and red symbols, respectively. The shaded regions denote the statistical uncertainty in the mass functions.

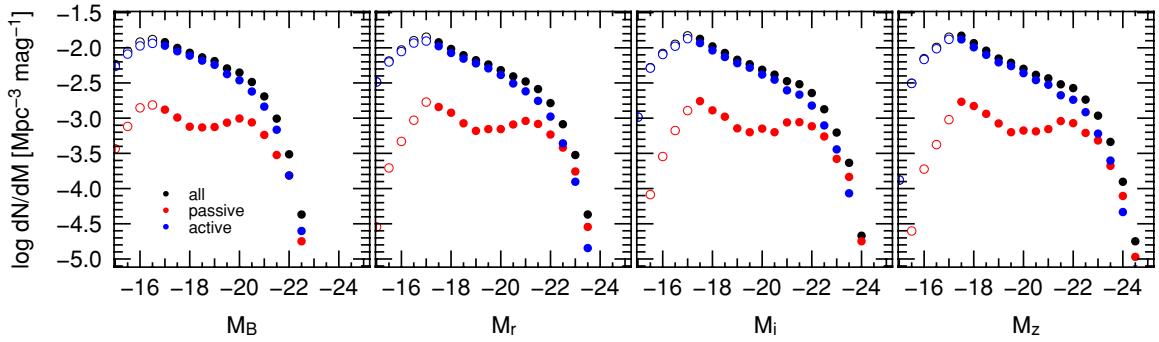

Figure 7. Luminosity function of galaxies (the number density of galaxies per comoving volume) in the rest frame B, r, i, and z bands at $z = 0.5$. Passive galaxies are marked in red, star-forming galaxies in blue, and all galaxies in black. Data points below the completeness limit are denoted by open symbols.

these differences are not large enough to change the shape of the mass function and the conclusions reached in this work in any significant way (also see Conroy et al. 2009 and Marchesini et al. 2009).

Could the mass function shape be affected by a failure to correctly model the very low M/L population? We plot the luminosity function of galaxies in the rest frame B, r, i, and z bands at $z \sim 0.5$ in Figure 7. The B-band luminosity function (LF) shows no bump in the blue or total galaxy populations; however a bump-like feature appears in the LF of blue and of all galaxies as one moves to redder filters, and is unmistakable in the z-band LF. So the dip and steep faint-end slope are present in luminosity functions redward of the rest frame B band and do not arise from converting luminosity to stellar mass via SED fitting.

5. DISCUSSION

5.1. Comparison to Previous Results

Before discussing possible interpretations of the more complicated mass function shape apparent in the COSMOS data, it is useful to compare our results to previous work with the aim of determining whether evidence for similar behavior has been found in other surveys. In Figure 8, we compare our mass function to a number of results from the literature and for later reference we include the halo mass function (Reed et al. 2007) where the halo masses have been multiplied by the global baryon fraction, $f_b = \Omega_b/\Omega_m$, taken from the *WMAP* five-year data (Dunkley et al. 2009). We show the $z \sim 0$ SDSS-based mass function by (Baldry et al. 2008) convolved with the photo-z error distributions as shown in Figure 4 and discussed in Section 4.1. We also plot the mass functions in the redshift range $0 < z < 1$ of active, passive, and all galaxies in the COSMOS survey selected at 3.6 μm by Ilbert et al. (2009b) using the same photometric redshifts as the present work. Finally, the total mass function selected at 3.6–4.5 μm by Pérez-González et al. (2008) is also plotted.

Where they overlap in mass, our mass functions agree very well with previous work, with some systematic differences stemming from differences in the underlying stellar population synthesis libraries and grids of SFHs (see Marchesini et al. 2009 and Conroy et al. 2009 for a systematic study on the influence of stellar population grid parameters on mass determinations). Of notable importance, though, is the fact that the bright components in our two-component fit to the mass function agree very well with the blue and the red sub-components in Ilbert et al. (2009b), despite (minor) differences in the definition of blue and red galaxies. This gives us confidence that the decomposition of the mass function into a bright and a faint component with six free parameters is not strongly degenerate. Specifically, both the mass scale of the bright components and their faint-end extrapolations are compatible with the single Schechter function fits to the more restricted data sets. We also confirm the buildup of the faint part of the red sequence at $z < 1$ observed by other groups (e.g., Bell et al. 2004, 2007; Bundy et al. 2006; Faber et al. 2007; Pérez-González et al. 2008; Ilbert et al. 2009b; Williams et al. 2009).

As we discuss further below, the apparent multi-component nature of the mass function has been discussed at low redshifts by Baldry et al. (2008) and Li & White (2009), and observed at some level in other high-z spectroscopic and hence significantly shallower studies of the COSMOS field (Pozzetti et al. 2009; Bolzonella et al. 2009). The advantage of the current analysis is that it probes to lower mass at redshifts beyond $z = 0.2$, thus allowing a larger dynamic range which for the first time at high-z reveals more complicated behavior, specifically the steepening of the faint-end slope and an additional population of faint red galaxies (also see Salimbeni et al. 2008). A similar steepening in the luminosity function below $M_i \sim -17$

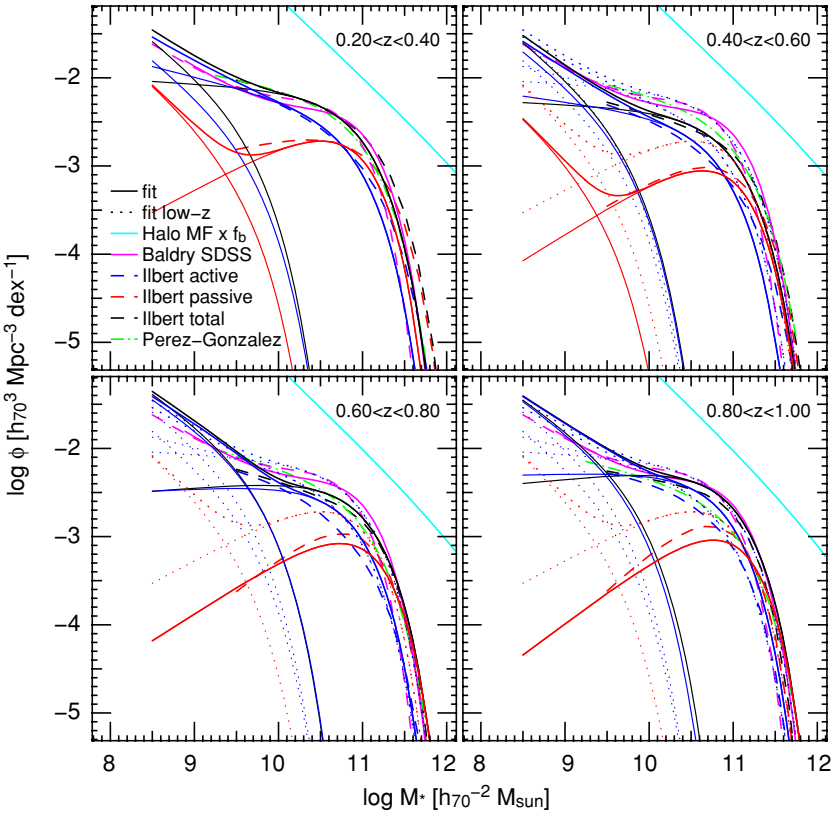

Figure 8. Comparison of the mass function deduced in this work with data from the literature. The mass function of passive galaxies is marked in red, that of star-forming galaxies in blue, and that of all galaxies in black. The solid lines show double Schechter function fits to the data (Equation (1); the thin lines show the individual bright and faint components of the double Schechter function). The fit at low z is repeated in higher z panels as dotted lines. The magenta line denotes the Baldry et al. (2008) $z \sim 0$ SDSS-based mass function convolved with the photo-z error distributions (see the text). The dashed blue, red, and black lines are the 3.6 μm-selected mass functions of active, passive, and all galaxies, respectively, in the COSMOS survey by Ilbert et al. (2009b). The green dash-dotted line is the mass function by Pérez-González et al. (2008). Additionally, we plot the Press–Schechter halo mass function scaled by the global baryon fraction f_b (Dunkley et al. 2009; *WMAP5*) in cyan.

has been convincingly detected recently in clusters (Driver et al. 1994; Trentham & Tully 2002; Hilker et al. 2003; Popesso et al. 2005, 2006), groups (Trentham & Tully 2002; Trentham et al. 2005; González et al. 2006), and in the field (Blanton et al. 2005). Baldry et al. (2008) find that the local galaxy stellar mass function steepens as well below $\log M/M_\odot \sim 9.5$ (also see Salucci & Persic 1999).

5.2. Halo Mass to Stellar Mass Relation

For the following discussion of the physical significance of the various morphological features of the mass function, it is useful to first place the mass function in the context of the halo mass function. We will do so by analyzing the halo mass versus galaxy stellar mass relation, noting that the more complicated shape of the stellar mass function also leads to a more complicated relation between galaxy stellar mass, M_g, and halo mass, M_h.

The relationship between the halo mass function and the galaxy (stellar) mass function can be written as

$$\phi_g(M_g, t) = \left|\frac{dM_h}{dM_g}\right| \phi_h(M_h, t). \quad (2)$$

Such a one-to-one correspondence between halo mass and galaxy stellar mass at some time, $M_h(M_g)$, can be found by requiring that the cumulative number density of halos above a given mass and galaxies above a corresponding stellar mass be equal (abundance matching),

$$\int_{M_g}^{\infty} \phi_g(M)dM = \int_{M_h}^{\infty} \phi_h(M)dM. \quad (3)$$

This approach has been shown to be sufficiently accurate to match the two-point correlation function of galaxies and halos (Conroy et al. 2006; Moster et al. 2009).

To obtain a more realistic picture of the halo masses of galaxies, we must include sub-halos in our abundance matching procedure, as halos (and hence their galaxies) may survive for considerable time. Analyzing high-resolution cosmological N-body simulations, Giocoli et al. (2008) and Angulo et al. (2009) provide fitting formulae for the number of sub-halos per host halo per logarithmic interval of sub-halo to host mass ratio, $dN_s/d\ln(M_s/M)$ (also see Gao et al. 2004). This quantity can be converted to a sub-halo mass function, $\phi_{\rm sub}(M_s)$, which is the more convenient quantity for our purposes by changing variables to obtain dN_s/dM_s, multiplying by the abundance of host halos, and integrating over host halo mass from M_s to infinity:

$$\phi_{\rm sub}(M_s) = \frac{dN_s}{dM_s} = \int_{M_s}^{\infty} \frac{dN_h}{dM_h}\frac{1}{M_s}\frac{dN_s}{d\ln(M_s/M)}dM. \quad (4)$$

This sub-halo mass function can then be added to the distinct halo mass function to obtain the total mass function that we use to match to the abundance of galaxies:

$$\phi(M) = \phi_{\rm distinct} + \phi_{\rm sub}. \quad (5)$$

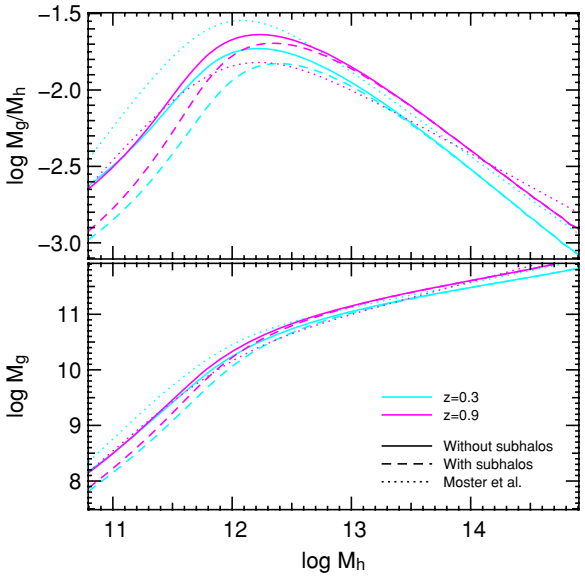

Figure 9. Stellar mass as a function of halo mass (bottom panel) and ratio between stellar mass and halo mass (top panel) at redshifts of $z = 0.3$ and $z = 0.9$ determined by abundance matching the galaxy stellar mass function to the halo mass function. The relation determined by Moster et al. (2009) is shown for comparison.

We note that we use the mass of the sub-halo at infall time, not the mass of the sub-halo at the time of observation for matching abundances. Most of the galaxy's properties will have been set by the time infall occurs (and shaped by the potential of the halo at that time) and galaxy growth is likely to slow down or even stop as soon as the galaxy becomes a satellite. This approach is motivated by models of galaxy formation that generically predict that stellar mass is tightly linked to the potential well in which the galaxy forms (Kauffmann et al. 1993; Cole et al. 1994; Somerville & Primack 1999). Sub-halos loose mass by tidal stripping, however their stars are more centrally concentrated and are not stripped until most of the dark matter has been lost. The relevant mass scale for sub-halos, therefore, is the virial mass at infall time.

We proceed using a halo mass function consisting of the distinct halo mass function by Reed et al. (2007) and the sub-halo abundance by Giocoli et al. (2008) processed through Equation (4). In Figure 9, we show the resulting relation between halo mass, M_h, and galaxy stellar mass, M_g at redshifts $z = 0.3$ and $z = 0.9$ obtained by abundance matching to our total galaxy stellar mass function. For comparison, we also show the relation obtained by Moster et al. (2009) by populating halos from N-body simulations with galaxies using semi-analytic methods and the requirement that the stellar mass function be reproduced.

Without accounting for substructure, $M_g(M_h)$ evolves relatively uniformly at all masses. With substructure, much less change in the relation at low mass is seen; there is little evolution in $M_g(M_h)$ from $z = 0.3$ to $z = 0.9$ at $\log M_h/M_\odot \lesssim 11.5$ (corresponding to $\log M_g/M_\odot \lesssim 9.5$, about the mass of the LMC). This is to be expected if the stellar content of low-mass halos is limited by feedback. There is evolution in the $M_g(M_h)$-relation at masses above M_*, where the stellar mass per halo mass increases by a factor of 1.23 from $z = 0.9$ to $z = 0.3$. The peak in star formation efficiency occurs in $\log M/M_\odot \sim 12.2$ halos and reaches 23% at $z = 0.3$ and 19% at $z = 0.9$; galaxy formation—if there is a monotonic relation between stellar mass and halo mass such as the one arrived at by abundance matching—is always an inefficient process.

While the flattening of the $M_g(M_h)$-relation above M_* (corresponding to the exponential cutoff in the galaxy mass function) is understood as an effect of the inefficiency of cooling in large halos (e.g., Rees & Ostriker 1977; White & Rees 1978), the steepening of the $M_g(M_h)$-relation at halo mass of $\log M/M_\odot \sim 11$ suggests another qualitative change in behavior of the feedback efficiency.

The $M_g(M_h)$-relation is fundamental to the process of galaxy formation within dark matter halos and understanding what shapes this relation is equivalent to understanding the galaxy stellar mass function. At this point we wish to remark that, due to the derivative factor dM_h/dM_g in Equation (2), or equivalently, the integral nature of the abundance matching relation in Equation (3), a single change of slope of $M_g(M_h)$ leads to a dip-bump structure in the inferred galaxy mass function, given a power-law halo mass function. The more abruptly the change of slope occurs, and the larger it is, the more pronounced the dip-bump feature in the mass function becomes. The mass function shape we observe, therefore, leads to an approximately double-power-law form of the $M_g(M_h)$-relation, as can be seen in Figure 9.

5.3. Interpreting the Shape of the Mass Function

There are several ways to interpret the shape of the total and type-dependent mass functions in COSMOS. Broadly speaking, we will concentrate on two interesting features, namely the "upturn" toward steeper faint-end slopes at low masses ($\log M/M_\odot \sim 9$) and an apparent "dip" or plateau at masses just above $\log M/M_\odot \sim 10$ that sets in below the traditional M^*. We note that even breaking down the mass function into these two components is, in itself, an interpretation since the steepening faint-slope alone may provide a viable explanation. As we discuss below, our interest in separately identifying the dip is motivated by comparisons to the underlying halo mass function, which is a strict power law at the relevant masses. In this context, the dip represents a suppression of the stellar mass associated with halos in this range; this is a consequence of a change in dM_h/dM_g such that there is a smaller change in the mass of galaxies per change in the mass of halos. The purpose of this section is, hence, to explore several physical mechanisms that may explain both the upturn and the dip and to speculate on the role of future observations in distinguishing them.

Using the zCOSMOS spectroscopic survey, Pozzetti et al. (2009) interpret the mass function they recover as being composed of early-type galaxies dominating the massive part and late-type galaxies dominating the less-massive part and contributing to the steep faint-end slope. They find that each of these components is well fitted by a Schechter function in the mass range they consider. Bolzonella et al. (2009) use the same sample to investigate the bimodality as a function of environment. The find that at $z \lesssim 0.5$, the shape of the galaxy stellar mass function in high- and low-density environments become extremely different, with high density regions showing a stronger bimodality. Also, Ilbert et al. (2009b) remark that the 3.6 μm-selected COSMOS mass function of all galaxies is not well fitted by a single Schechter function. They prefer the sum of their (Schechter) fits to the red and blue galaxies to describe the whole population, as this reproduces the dip at intermediate mass of $\log M \sim 10$ and $z \lesssim 0.6$ they observe. Due to the IRAC selection, they do not reach faint enough limits to detect the steep faint-end slope or the bimodal structure at higher z. We overplot the data from the FDF (Drory et al. 2005) at $z = 0.5$ in Figure 5 and note

that the bimodality is visible there as well, although Drory et al. (2005) do not discuss it because a single Schechter fit seemed adequate at the time (apart from the data point at $\log M = 11$, which comes out too high).

We emphasize that we see even more structure in the mass function than observed in the works discussed above; those studies only detect a dip in the total mass function and interpret its origin as being due to the superposition of active and passive populations which by themselves are unimodal. In this paper, we detect a significant change in slope in the mass functions of active galaxies as well as a marked bimodality in the mass function of passive galaxies.

As mentioned above, previous work has attributed the two-component nature of the mass function to a superposition of a (unimodal) blue galaxy population modeled as a Schechter function and a red galaxy population, also modeled as a Schechter function but with a larger characteristic mass. In this picture, the bimodality arises through the transformation of blue galaxies into red galaxies in a process that must be linked to the mass evolution of a transitioning galaxy to deplete the dip and create a bump at $M \sim M^*$. In contrast, we find that the blue galaxy population by itself shows a dip signature and a steepening of the power-law slope, which can be interpreted as arising from a bimodal distribution. In fact, both the red and the blue populations in Figure 5 can be interpreted as bimodal. However, the bimodality in the blue population seems to be more pronounced at high z compared to low z: it becomes weaker as redshift decreases. This effect can also be seen in the χ^2 values reported in Table 3. Indeed, the best χ^2 values for single Schechter fits are obtained for the blue component at low redshift ($\chi^2_{\rm single} = 7.0$). The signature of the bimodality (the dip at intermediate mass, or the bump at around M^*) "moves" from the blue population at high z to the red population at low z. This is likely because some of the blue galaxies that make up the bump around M^* in the blue mass function turn red with time (e.g., Bell et al. 2004; Bundy et al. 2006; Faber et al. 2007; Williams et al. 2009).

The fact that the blue mass function is itself bimodal at $z \sim 1$ implies that the shape of the total mass function predates the emergence of the red sequence. We, therefore, suggest that the physical explanation must be a mass-dependent effect or mechanism that is largely separate from the process that transforms star-forming disks into passive spheroidals. In other words, this suggests a new dichotomy in the galaxy distribution besides the well-known red–blue distinction. We will follow this hypothesis in the following, using the behavior of blue galaxies to stand in for interpretations of the full population and returning to red systems in the subsequent section.

5.3.1. Blue Galaxies

Before discussing possible physical explanations, we note that among star-forming, blue galaxies, there is an interesting separation between (giant) spirals of Hubble types Sa–Scd that dominate the mass function at the massive end and make up the majority of objects above the dip, and dwarf galaxies of Hubble types Sd–Sm/Im that dominate the less-massive, power-law part of the blue galaxy mass function. Disk parameters such as disk radius and luminosity remain roughly constant (with a large spread) along the Hubble sequence at types Sa-Scd. For types later than Sd galaxies, the Hubble sequence turns into a luminosity sequence, with later type morphologies corresponding to smaller and less-massive galaxies (see, for example, the review by Roberts & Haynes 1994 and references therein). It is also worth noting that Disk galaxies without a significant bulge component exist (e.g., Hubble-type Sd and later) and can be accurately characterized as pure disk systems, harboring at most a nuclear star cluster. May we tentatively identify this distinction in disk properties with the two components in the blue population's mass function? If so, the physical processes discussed below must also account for these morphological differences.

Star Formation Efficiency. The dip in the stellar mass function corresponds to a change in the stellar mass versus halo mass relation such that there is a smaller change in the number of galaxies when measured against the power-law shape of the halo mass abundance (Figures 8 and 9). It is possible that this deficit arises from a change in the efficiency of star formation with mass. In this interpretation, the *baryonic* mass function, if it could be observed, would show a close to power-law shape below M^*, indicating a more smoothly varying fraction of $M_{\rm baryon}/M_{\rm halo}$ with $M_{\rm halo}$. For this to still be the case at later cosmic times, we must also require that the fraction of gas retained by any halo in the interesting mass range must be a smooth function of halo mass and also that this fraction not be too small. Then, a decrease in SFR efficiency below a given mass scale (say $\log M/M_\odot \sim 10$) would lead to an increasing gas fraction, $f_{\rm gas}$, at lower masses and a *decreasing* stellar mass fraction. This is analogous to the break in the Tully–Fisher relation (Tully & Fisher 1977) where galaxies with $V_c \lesssim 90$ km s^{-1} fall below the relation defined by more massive galaxies. If plotted against total disk mass, $M_{\rm gas} + M_{\rm star}$, instead of luminosity, a single relation is restored with $M_{\rm gas} + M_{\rm star} \sim V_c^4$ (McGaugh et al. 2000). The decrease in $f_{\rm gas}$ as a function of M has been observed. Thus, galaxies with baryonic masses near $\log M/M_\odot \sim 10$ would have observed M several factors lower, thereby creating a dip in the stellar mass function at $\log M/M_\odot \sim 10$, and leading to a steepening below $\log M/M_\odot \sim 9$.

Using a simple fitting spline to observations of $f_{\rm gas}(M)$ compiled by Hopkins et al. (2009c) including data from Bell & de Jong (2001), Kannappan (2004), and McGaugh (2005), we transform the total stellar mass function at $z = 0.3$ into an approximate baryonic mass function. The gas fraction hereby is defined as the ratio of gas mass to stellar plus gas mass, $f_{\rm gas} = M_{\rm gas}/(M_{\rm gas} + M_{\rm star})$. We plot the results in Figure 10.

Using the observed gas fraction as a function of mass, the dip in the mass function can be lessened, but not removed. However, as expected, an appropriate *assumption* for $f_{\rm gas}(M)$ leads to baryonic mass functions in which the dip can be "straightened" out (dot-dashed line). However, the amount of $f_{\rm gas}(M)$ required is about a factor of 2 higher than current low-z observations (dashed line). This comparison involves several large uncertainties, but plausibly, the difference could be made up for in a warm phase that is not easily detected (Cen & Ostriker 1999; Davé et al. 2001; Cen & Ostriker 2006). One would also expect $f_{\rm gas}$ to increase with redshift in line with rising SFRs. We are able to conclude that it is at least *possible* that the dip in the stellar mass function reflects a mass dependence in the ability for baryons to cool and form stars.

What causes this mass-dependent SFR efficiency? We note that the deviation of the stellar mass function from power-law form at $\log M/M_\odot \sim 9$–10 is close to the scale where supernova feedback becomes less important, $V_c \sim 100$ km s^{-1} (Dekel & Silk 1986; Benson et al. 2003). As long as supernova feedback is efficient in regulating the conversion of gas into stars, the ratio of

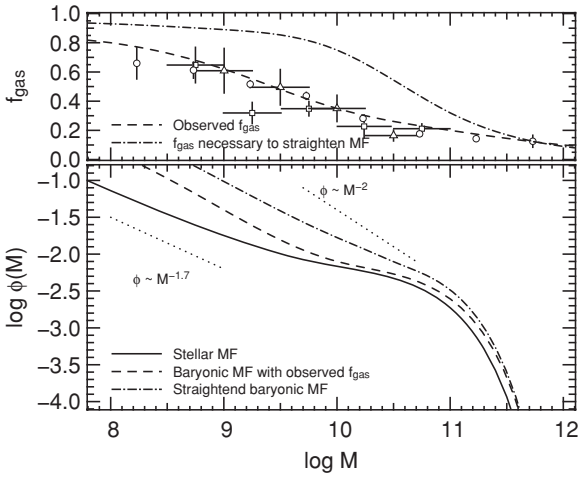

Figure 10. Top panel shows the gas fraction, $f_{\rm gas}$, as a function of stellar mass. The data are taken from a compilation by Hopkins et al. (2009c), including Bell & de Jong (2001; triangles), Kannappan (2004; circles), and McGaugh (2005; squares). A spline interpolation to the data is shown as a dashed line. The gas fraction necessary to remove the dip structure in the mass function is shown as a dash-dotted line. In the bottom panel, we plot the total stellar mass function at $z = 0.3$ and the baryonic mass function obtained by applying the gas fractions from the top panel. Power-law slopes of $\phi \sim M^{-2}$ for the halo mass function and $\phi \sim M^{-1.7}$ for the stellar mass function are plotted for reference.

stellar mass to halo mass is set by the scaling relation of feedback efficiency with halo mass (or circular velocity). Once the (dark matter (DM)) potential is deep enough that supernova feedback can no longer remove significant amounts of gas from the halo, the attainable ratio of stellar mass to dark matter mass becomes larger as a larger fraction of the gas in the halo can cool to form stars. As a consequence, the stellar mass function deviates upward from its power-law form. At the massive end, the stellar mass is limited by the cooling timescale becoming too large and the ratio of stellar mass to dark mass decreases again sharply causing the exponential cutoff in the stellar mass function (Rees & Ostriker 1977; White & Rees 1978). The transition from SFR efficiency suppressed by supernovae feedback to peak SFR efficiency may therefore lead to the observed dip in the stellar mass function.

There are two potential tests for this scenario. The most obvious is to seek better measures of $f_{\rm gas}$ as a function of M and redshift, but such observations remain challenging. A second test is to determine whether the mass scale that defines the dip evolves with redshift. Because we expect $f_{\rm gas}$ to be higher in more massive galaxies at early times (since at $z > 1$ many more are likely to be rapidly forming stars), the dip in the stellar mass function should move to higher masses at early times as well. Unfortunately, the mass functions presented here are likely to be too affected by cosmic variance to robustly measure redshift evolution in the dip feature, but future data sets will be able to overcome this problem. Also, a more rigorous analysis taking into account cosmological gas accretion as well as a realistic feedback prescription and outflow model is needed, but is beyond the scope of this paper.

Hierarchical assembly. Another possibility is that the dip at $\log M \sim 10$ and the bump around M^* are formed by a depletion of stellar and gas mass at intermediate mass resulting from a pile-up of the end-products of mass-dependent assembly around M^*. In this scenario, both the stellar and baryonic mass functions would exhibit dips at $\log M \sim 10$ because the assembly of baryonic mass is accelerated at a certain scale.

It is known that the halo–halo merger rate depends very weakly on mass (Fakhouri & Ma 2008). However, if the stellar mass, or in this case, baryonic mass fraction, peaks in halos at a given mass scale—perhaps as a result of the SFR feedback discussed above—the resulting merger rate in terms of stellar mass, M, or baryonic mass, $M_{\rm baryons}$, can be enhanced near this scale (Bundy et al. 2009; Stewart 2009; Hopkins et al. 2009a) and strengthen the dip feature. This is because the dynamical friction timescale (and hence the merger timescale) depends firstly on the mass ratio of the merging systems (e.g., Boylan-Kolchin et al. 2008 and references therein). Low mass ratio mergers happen only after a long time, and one-to-one mergers happen quickly. At low mass, one-to-one mergers in DM correspond to minor mergers in baryons and hence the baryonic content of a halo assembles more slowly than the halo. This is due to the steep relation between stellar mass, M_g, and halo mass, M_h, below M^* (see Figure 9). At masses near and just above the scale at which $M_g(M_h)$ flattens, more frequent minor halo mergers can host one-to-one baryonic mergers and thus the baryonic assembly rates increase markedly. At even higher mass scales, above the flattening at M^* of the $M_h(M_g)$-relation, the infalling galaxy is much more likely to become and stay a satellite, even if the baryonic mass ratio is close to one. At this point, the baryonic merger rate drops again.

As a result, low stellar (baryonic) mass galaxies get depleted more rapidly in one-to-one mergers, and pile-up around the M^* mass scale ($M^* \sim 10^{11}\,M_\odot$). This scenario also suggests that the two populations of galaxies might be thought of as central galaxies occupying the bump with an increasing fraction of satellite galaxies at lower masses that possibly form the second, faint, component of the mass function, leading to a steepening of the low-mass end of the mass function. Such satellites in a galaxy or group halo would orbit for a long time before merging and hence remain visible as individual galaxies.

If this enhanced assembly scenario were important, it would also indicate that many major mergers between star-forming (disk) galaxies must not lead to a final destruction of the disk and truncation of star formation as the bump signature is already apparent in the blue galaxy population at $z \sim 1$. Such mergers must produce a remnant that is still a blue star-forming disk galaxy. Such outcomes of mergers seem possible if the gas fraction is large (Springel & Hernquist 2005; Robertson et al. 2006; Governato et al. 2007; Hopkins et al. 2009b). Also, we would expect the dip feature to deepen with time but, in contrast with SFR scenario above, remain relatively fixed with respect to mass.

Steepening Faint-end Slope. So far, we have focused on the dip in the stellar mass function. We now turn to the steep slopes at the low-mass end. To the extent that this feature is unrelated to the dip forming process mentioned above, we can consider several possibilities. To begin with, many authors interpret the faint-end slope as rising to the maximum set by the halo mass function (with a value of -2). Such behavior is expected if feedback processes that regulate the star formation efficiency become increasingly independent of $M_{\rm halo}$ below some scale. At low masses, for example, supernova feedback may so dominate over the ability of halos to retain gas, that the effective gas or stellar mass fraction becomes a constant, independent of halo mass.

5.3.2. Red Galaxies

We now turn to the behavior of the red galaxy mass function. In the redshift bins $z = 0.5$ and $z = 0.3$, where the faint

red component of the mass function is sampled well, the number density of all galaxies at $M \lesssim 9.5$ does not change much (Figure 8 and Table 3). Yet, the number density of faint red galaxies increases by 0.45 dex, a combined effect of the normalization increasing from $\phi_f(z = 0.5) = 0.28$ to $\phi_f(z = 0.3) = 0.49$ and the characteristic mass of the low-mass component increasing from $M^*_f(z = 0.5) = 9.41$ to $M^*_f(z = 0.3) = 9.54$. This evolution in faint red galaxies is nearly perfectly mirrored by a decrease in number of faint blue galaxies. As we have noted above, the faint-end slope of the active and the passive population is consistent with being equal.

The similarity of the steep faint-end slopes of the active and faint passive populations and their reciprocal change in number density is suggestive of the latter originating from the former by shutting off star formation. It is very tempting to identify these two faint galaxy populations sharing the same steep faint-end slope with Sm/Im/dIrr galaxies, and faint spheroidal galaxies, respectively (Kormendy 1985). It is established that passively evolving dwarf galaxies cluster around massive galaxies (Zehavi et al. 2005; Haines et al. 2006, 2007; Carlberg et al. 2009), and tidal interactions or ram pressure stripping may well lead to quenching and some subsequent phase mixing turning Sm/Im galaxies into faint spheroidal galaxies (Mayer et al. 2001; Grebel et al. 2003; Haines et al. 2007). Also, McCracken et al. (2008) finds that in the CFHTLS in the redshift bin $0.2 < z < 0.6$, the clustering amplitude for faint red galaxies is actually higher than that of bright red galaxies, which is to be expected in our interpretation.

6. SUMMARY

Following on previous studies of the stellar mass function in the COSMOS field (Ilbert et al. 2009b; Pozzetti et al. 2009; Bolzonella et al. 2009), we present a new analysis of this data set that provides mass functions to fainter limits than has been previously probed at $z \lesssim 1$. The resulting increase in dynamic range allows us to characterize and study features in the shape of the stellar mass function that deviate from a single Schechter function. We have tested whether these features could be introduced by a variety of systematic effects including both catastrophic photometric redshift errors as well as increasing photo-z uncertainty at low masses, differences in the way stellar population models account for TP-AGB stars, and the ability of stellar mass codes to convert from luminosity to mass. We conclude that our results are robust to these effects, although the data are still limited by cosmic variance. Our key results follow.

1. Neither the total nor the red (passive) or blue (star-forming) galaxy stellar mass functions can be well fit with a single Schechter function once the mass completeness limit of the sample probes below roughly $3 \times 10^9\,M_\odot$. We model this more complicated behavior using a double Schechter function with six free parameters, and present the fitting results for four redshift bins to $z = 1$.
2. The bimodal nature of the mass function is *not* solely a result of the blue/red dichotomy. Indeed, the blue mass function is already bimodal at $z \sim 1$. This suggests a new two-component model for galaxy formation that predates the appearance of the red sequence.
3. We propose two interpretations for this bimodal distribution, focusing on the "dip" in the blue mass function at $\sim 10^{10}\,M_\odot$. If the gas fraction increases at lower stellar masses, galaxies with $M_{\rm baryon} \sim 10^{10}\,M_\odot$ would shift to lower stellar masses, creating the observed dip. This would indicate a change in SFR efficiency, perhaps arising from the influence of supernovae feedback which likely sets in below scales of $\sim 10^{10}\,M_\odot$. In this picture, the baryonic mass function should not show a dip. Using published (cold) gas fractions as a function of stellar mass, we show that cold gas alone is not sufficient to eliminate the dip in the baryonic mass function, but that the addition of the hard to detect warm gas could potentially flatten out the baryonic mass function considerably.
4. Alternatively, the dip could be created by an enhancement of the galaxy assembly rate at $\sim 10^{11}\,M_\odot$, a phenomenon that naturally arises if the baryon fraction peaks at $M_{\rm halo} \sim 10^{12}\,M_\odot$. In this scenario, we would identify the galaxies occupying the bump around M_* with central galaxies and the increasing fraction of satellite galaxies at lower mass with the second, fainter, component of the mass function and, in particular, the steep faint-end slope.
5. The low-mass end of the blue and total mass functions exhibit a steeper slope than has been detected in previous work. This can be interpreted as a *steepening* slope, one that may increasingly approach the halo mass function value of -2.
6. While the dip feature is apparent in the total mass function at all redshifts, it appears to shift from the blue to the red population, likely as a result of transforming high-mass blue galaxies into red ones.
7. At the same time, we detect a drastic upturn in the number of low-mass red galaxies. Their increase with time seems to reflect a decrease in the number blue systems and so we tentatively associate them with satellite (dwarf spheroidal) galaxies that have undergone quenching due to environmental processes.

While the broad dynamic range of the COSMOS data set allows us to begin to characterize some of the more subtle features of the stellar mass function, the single COSMOS field is still limited by cosmic variance. Future work over several fields will verify the trends here and shed light on possible interpretations by constraining how these features evolve with redshift.

We thank R. Angulo, R. Bender, R. Ellis, P. F. Hopkins, S. Khochfar, and J. Tinker for stimulating discussions. We also thank P. F. Hopkins for providing gas mass fractions in electronic form. We thank the COSMOS collaboration for granting us access to their catalogs; and we gratefully acknowledge the contributions of the entire COSMOS team that have made this work possible. More information on the COSMOS survey is available at http://www.astro.caltech.edu/cosmos. A.L. acknowledges support from the Chamberlain Fellowship at LBNL and from the Berkeley Center for Cosmological Physics. H.J.McC. is supported by ANR grant "ANR-07-BLAN-0228."

REFERENCES

Angulo, R. E., Lacey, C. G., Baugh, C. M., & Frenk, C. S. 2009, MNRAS, 399, 983
Arnouts, S., et al. 2007, A&A, 476, 137
Baldry, I. K., Glazebrook, K., & Driver, S. P. 2008, MNRAS, 388, 945
Bell, E. F., & de Jong, R. S. 2001, ApJ, 550, 212
Bell, E. F., McIntosh, D. H., Katz, N., & Weinberg, M. D. 2003, ApJS, 149, 289
Bell, E. F., Zheng, X. Z., Papovich, C., Borch, A., Wolf, C., & Meisenheimer, K. 2007, ApJ, 663, 834
Bell, E. F., et al. 2004, ApJ, 608, 752
Benson, A. J., Bower, R. G., Frenk, C. S., Lacey, C. G., Baugh, C. M., & Cole, S. 2003, ApJ, 599, 38

Blanton, M. R., Lupton, R. H., Schlegel, D. J., Strauss, M. A., Brinkmann, J., Fukugita, M., & Loveday, J. 2005, ApJ, 631, 208
Bolzonella, M., et al. 2009, arXiv:0907.0013
Borch, A., et al. 2006, A&A, 453, 869
Bouwens, R. J., Illingworth, G. D., Blakeslee, J. P., & Franx, M. 2006, ApJ, 653, 53
Boylan-Kolchin, M., Ma, C.-P., & Quataert, E. 2008, MNRAS, 383, 93
Brinchmann, J., Charlot, S., White, S. D. M., Tremonti, C., Kauffmann, G., Heckman, T., & Brinkmann, J. 2004, MNRAS, 351, 1151
Brinchmann, J., & Ellis, R. S. 2000, ApJ, 536, L77
Bruzual, G. 2007, in ASP Conf. Ser. 374, From Stars to Galaxies: Building the Pieces to Build Up the Universe, ed. A. Vallenari et al. (San Francisco, CA: ASP), 303
Bruzual, G., & Charlot, S. 2003, MNRAS, 344, 1000
Bundy, K., Ellis, R. S., & Conselice, C. J. 2005, ApJ, 625, 621
Bundy, K., Fukugita, M., Ellis, R. S., Targett, T. A., Belli, S., & Kodama, T. 2009, ApJ, 697, 1369
Bundy, K., et al. 2006, ApJ, 651, 120
Calzetti, D., Armus, L., Bohlin, R. C., Kinney, A. L., Koornneef, J., & Storchi-Bergmann, T. 2000, ApJ, 533, 682
Capak, P., et al. 2007, ApJS, 172, 99
Carlberg, R. G., Sullivan, M., & LeBorgne, D. 2009, ApJ, 694, 1131
Cen, R., & Ostriker, J. P. 1999, ApJ, 514, 1
Cen, R., & Ostriker, J. P. 2006, ApJ, 650, 560
Chabrier, G. 2003, PASP, 115, 763
Chapman, S. C., Blain, A. W., Smail, I., & Ivison, R. J. 2005, ApJ, 622, 772
Cohen, J. G. 2002, ApJ, 567, 672
Cole, S., Aragon-Salamanca, A., Frenk, C. S., Navarro, J. F., & Zepf, S. E. 1994, MNRAS, 271, 781
Cole, S., et al. 2001, MNRAS, 326, 255
Conroy, C., Gunn, J. E., & White, M. 2009, ApJ, 699, 486
Conroy, C., Wechsler, R. H., & Kravtsov, A. V. 2006, ApJ, 647, 201
Conselice, C. J., Blackburne, J. A., & Papovich, C. 2005, ApJ, 620, 564
Daddi, E., et al. 2007, ApJ, 670, 156
Davé, R., et al. 2001, ApJ, 552, 473
Davis, M., et al. 2003, Proc. SPIE, 4834, 161
Dekel, A., & Silk, J. 1986, ApJ, 303, 39
Dickinson, M., Papovich, C., Ferguson, H. C., & Budavári, T. 2003, ApJ, 587, 25
Driver, S. P., Phillipps, S., Davies, J. I., Morgan, I., & Disney, M. J. 1994, MNRAS, 268, 393
Drory, N., & Alvarez, M. 2008, ApJ, 680, 41
Drory, N., Bender, R., Feulner, G., Hopp, U., Maraston, C., Snigula, J., & Hill, G. J. 2004a, ApJ, 608, 742
Drory, N., Bender, R., & Hopp, U. 2004b, ApJ, 616, L103
Drory, N., Bender, R., Snigula, J., Feulner, G., Hopp, U., Maraston, C., Hill, G. J., & Mendes de Oliveira, C. 2001, ApJ, 562, L111
Drory, N., Salvato, M., Gabasch, A., Bender, R., Hopp, U., Feulner, G., & Pannella, M. 2005, ApJ, 619, L131
Dunkley, J., et al. 2009, ApJS, 180, 306
Elsner, F., Feulner, G., & Hopp, U. 2008, A&A, 477, 503
Eyles, L. P., Bunker, A. J., Ellis, R. S., Lacy, M., Stanway, E. R., Stark, D. P., & Chiu, K. 2007, MNRAS, 374, 910
Faber, S. M., et al. 2007, ApJ, 665, 265
Fakhouri, O., & Ma, C.-P. 2008, MNRAS, 386, 577
Fontana, A., et al. 2003, ApJ, 594, L9
Fontana, A., et al. 2004, A&A, 424, 23
Fontana, A., et al. 2006, A&A, 459, 745
Gao, L., White, S. D. M., Jenkins, A., Stoehr, F., & Springel, V. 2004, MNRAS, 355, 819
Giocoli, C., Tormen, G., & van den Bosch, F. C. 2008, MNRAS, 386, 2135
Glazebrook, K., et al. 2004, Nature, 430, 181
González, R. E., Lares, M., Lambas, D. G., & Valotto, C. 2006, A&A, 445, 51
Governato, F., Willman, B., Mayer, L., Brooks, A., Stinson, G., Valenzuela, O., Wadsley, J., & Quinn, T. 2007, MNRAS, 374, 1479
Grazian, A., et al. 2007, A&A, 465, 393
Grebel, E. K., Gallagher, J. S., III, & Harbeck, D. 2003, AJ, 125, 1926
Haines, C. P., Gargiulo, A., La Barbera, F., Mercurio, A., Merluzzi, P., & Busarello, G. 2007, MNRAS, 381, 7
Haines, C. P., La Barbera, F., Mercurio, A., Merluzzi, P., & Busarello, G. 2006, ApJ, 647, L21
Hilker, M., Mieske, S., & Infante, L. 2003, A&A, 397, L9
Hopkins, P. F., Cox, T. J., Younger, J. D., & Hernquist, L. 2009b, ApJ, 691, 1168
Hopkins, P. F., et al. 2009a, arXiv:0906.5357
Hopkins, P. F., et al. 2009c, MNRAS, 397, 802
Ilbert, O., et al. 2009a, ApJ, 690, 1236
Ilbert, O., et al. 2009b, arXiv:0903.0102
Kannappan, S. J. 2004, ApJ, 611, L89
Kannappan, S. J., & Gawiser, E. 2007, ApJ, 657, L5
Kauffmann, G., White, S. D. M., & Guiderdoni, B. 1993, MNRAS, 264, 201
Kauffmann, G., et al. 2003, MNRAS, 341, 33
Kormendy, J. 1985, ApJ, 295, 73
Leauthaud, A., et al. 2007, ApJS, 172, 219
Le Fèvre, O., et al. 2005, A&A, 439, 845
Li, C., & White, S. D. M. 2009, MNRAS, 398, 2177
Lilly, S. J., et al. 2007, ApJS, 172, 70
Lilly, S. J., et al. 2009, ApJS, 184, 218
Maraston, C. 2005, MNRAS, 362, 799
Maraston, C., Daddi, E., Renzini, A., Cimatti, A., Dickinson, M., Papovich, C., Pasquali, A., & Pirzkal, N. 2006, ApJ, 652, 85
Marchesini, D., van Dokkum, P. G., Forster Schreiber, N. M., Franx, M., Labbé, I., & Wuyts, S. 2009, ApJ, 701, 1765
Mayer, L., Governato, F., Colpi, M., Moore, B., Quinn, T., Wadsley, J., Stadel, J., & Lake, G. 2001, ApJ, 559, 754
McCracken, H. J., Ilbert, O., Mellier, Y., Bertin, E., Guzzo, L., Arnouts, S., Le Fèvre, O., & Zamorani, G. 2008, A&A, 479, 321
McCracken, H. J., et al. 2009, arXiv:0910.2705
McGaugh, S. S. 2005, ApJ, 632, 859
McGaugh, S. S., Schombert, J. M., Bothun, G. D., & de Blok, W. J. G. 2000, ApJ, 533, L99
Meneux, B., et al. 2009, A&A, 505, 463
Moster, B. P., Somerville, R. S., Maulbetsch, C., van den Bosch, F. C., Macció, A. V., Naab, T., & Oser, L. 2009, arXiv:0903.4682
Pannella, M., Hopp, U., Saglia, R. P., Bender, R., Drory, N., Salvato, M., Gabasch, A., & Feulner, G. 2006, ApJ, 639, L1
Pannella, M., et al. 2009, arXiv:0906.2810
Panter, B., Heavens, A. F., & Jimenez, R. 2004, MNRAS, 355, 764
Pérez-González, P. G., Gallego, J., Zamorano, J., Alonso-Herrero, A., Gil de Paz, A., & Aragón-Salamanca, A. 2003, ApJ, 587, L27
Pérez-González, P. G., et al. 2008, ApJ, 675, 234
Polletta, M., et al. 2007, ApJ, 663, 81
Popesso, P., Biviano, A., Böhringer, H., & Romaniello, M. 2006, A&A, 445, 29
Popesso, P., Böhringer, H., Romaniello, M., & Voges, W. 2005, A&A, 433, 415
Pozzetti, L., et al. 2007, A&A, 474, 443
Pozzetti, L., et al. 2009, arXiv:0907.5416
Reed, D. S., Bower, R., Frenk, C. S., Jenkins, A., & Theuns, T. 2007, MNRAS, 374, 2
Rees, M. J., & Ostriker, J. P. 1977, MNRAS, 179, 541
Reichardt, C., Jimenez, R., & Heavens, A. F. 2001, MNRAS, 327, 849
Roberts, M. S., & Haynes, M. P. 1994, ARA&A, 32, 115
Robertson, B., Bullock, J. S., Cox, T. J., Di Matteo, T., Hernquist, L., Springel, V., & Yoshida, N. 2006, ApJ, 645, 986
Robin, A. C., et al. 2007, ApJS, 172, 545
Rudnick, G., et al. 2003, ApJ, 599, 847
Rudnick, G., et al. 2006, ApJ, 650, 624
Salimbeni, S., et al. 2008, A&A, 477, 763
Salpeter, E. E. 1955, ApJ, 121, 161
Salucci, P., & Persic, M. 1999, MNRAS, 309, 923
Schechter, P. 1976, ApJ, 203, 297
Somerville, R. S., & Primack, J. R. 1999, MNRAS, 310, 1087
Springel, V., & Hernquist, L. 2005, ApJ, 622, L9
Stark, D. P., Bunker, A. J., Ellis, R. S., Eyles, L. P., & Lacy, M. 2007, ApJ, 659, 84
Stasińska, G., Mateus, A., Jr., Sodré, L., Jr., & Szczerba, R. 2004, A&A, 420, 475
Stewart, K. R. 2009, arXiv:0902.2214
Stringer, M. J., Benson, A. J., Bundy, K., Ellis, R. S., & Quetin, E. L. 2009, MNRAS, 393, 1127
Trentham, N., Sampson, L., & Banerji, M. 2005, MNRAS, 357, 783
Trentham, N., & Tully, R. B. 2002, MNRAS, 335, 712
Tully, R. B., & Fisher, J. R. 1977, A&A, 54, 661
Tully, R. B., Pierce, M. J., Huang, J.-S., Saunders, W., Verheijen, M. A. W., & Witchalls, P. L. 1998, AJ, 115, 2264
White, S. D. M., & Rees, M. J. 1978, MNRAS, 183, 341
Williams, R. J., Quadri, R. F., Franx, M., van Dokkum, P., & Labbé, I. 2009, ApJ, 691, 1879
Yan, H., Dickinson, M., Giavalisco, M., Stern, D., Eisenhardt, P. R. M., & Ferguson, H. C. 2006, ApJ, 651, 24
Zehavi, I., et al. 2005, ApJ, 630, 1